## RESEARCH ARTICLE

# Single-Pixel Photoacoustic Microscopy with Speckle Illumination

Antonio M. Caravaca-Aguirre[1], Florian Poisson[1], Dorian Bouchet[1], Nicolino Stasio[2], Philippe Moreau[1], Irene Wang[1], Edward Zhang[3,4], Paul Beard[3,4], Claire Prada[5], Christophe Moser[6], Demetri Psaltis[2], Ori Katz[7], and Emmanuel Bossy[1]*

[1]Université Grenoble Alpes, CNRS, LIPhy, 38000 Grenoble, France. [2]Laboratory of Optics, School of Engineering, EPFL, Lausanne, Switzerland. [3]Department of Medical Physics and Biomedical Engineering, University College London, London, UK. [4]Wellcome/EPSRC Centre for Interventional and Surgical Sciences, University College London, London, UK. [5]Institut Langevin, ESPCI, PSL University, CNRS, Paris, France. [6]Laboratory of Applied Photonics Devices, School of Engineering, EPFL, Lausanne, Switzerland. [7]Department of Applied Physics, Hebrew University of Jerusalem, Jerusalem, Israel.

*Address correspondence to: emmanuel.bossy@univ-grenoble-alpes.fr

Wide-field optical-resolution microscopy with structured illumination and single-pixel detection has been the topic of a number of research investigations. Its advantages over point scanning approaches are many and include a faster acquisition rate for sparse samples, sectioning, and super-resolution features. Initially introduced for fluorescence imaging, structured illumination approaches have been adapted and developed for many other imaging modalities. In this paper, we illustrate how speckle illumination, as a particular type of structured illumination, can be exploited to perform optical-resolution photoacoustic microscopy with a single-pixel imaging approach. We first introduce the principle of single-pixel detection applied to photoacoustic imaging and then illustrate in 2 different situations how photoacoustic images may be computationally reconstructed from speckle illumination: In the first situation where the speckle patterns are known through a prior calibration, various reconstruction approaches may be implemented, which are demonstrated experimentally through both scattering layers and multimode optical fibers; in the second situation where the speckle patterns are unknown (blind structured illumination), the so-called memory effect can be harnessed to produce calibration-free photoacoustic images, following the approach initially proposed for fluorescence imaging through thin scattering layers.

## Introduction

Photoacoustic imaging, also called optoacoustic imaging, is an imaging technique that provides optical contrast via the detection of sound. It is based on the photoacoustic effect, defined as the emission of acoustic waves following the absorption of light by optical absorbers through thermoelastic stress generation. Although the photoacoustic effect was discovered by Graham Bell more than a century ago [1,2], the topic of biomedical photoacoustic imaging has undergone a tremendous development over the past 2 decades [3–6]. One feature unique to photoacoustic imaging is that it can provide images of optical absorbers embedded deep in multiply scattering media (such as blood vessels in biological tissue) with the resolution of ultrasound. In this regime where light is multiply scattered, photoacoustic imaging is referred to as acoustic-resolution photoacoustic imaging (AR-PAM). In practice, the depth-to-resolution ratio of AR-PAM in biological tissue is on the order of 200 [3,4]: As

an example, optical images with a resolution of 100 μm may be obtained at a depth of around 2 cm, where purely optical techniques such as diffuse optical tomography would be limited to a centimeter resolution. Beyond this feature, unique among optical imaging techniques, another important feature of photoacoustic imaging is its specificity to optical absorption (as opposed to optical scattering), as pressure waves are generated only through optical absorption. In parallel to imaging at depth with the resolution of ultrasound, photoacoustic imaging has thus also been applied to the field of optical-resolution microscopy [7]. In a similar way to all-optical microscopy techniques such as fluorescence scanning microscopy, fluorescence sensing is simply replaced by acoustic sensing. In its most common implementation, optical-resolution photoacoustic microscopy (often referred to as OR-PAM) is based on raster scanning a focus beam over a 2-dimensional (2D) sample [7], and the image is straightforwardly built from the acoustic energy measured at each scan step, similarly to scanning fluorescence microscopy. Importantly, in

OR-PAM, the resolution is dictated by the resolution of the illumination pattern, while the detection of sound is performed with a single-element transducer.

While scanning approaches are the most straightforward ones, they have several limitations, including long acquisition times (proportional to the field of view) and a resolution limited by the optical diffraction limit and depth dependence. For fluorescence imaging, several alternative to scanning microscopy have been proposed to tackle its limitations, particularly techniques based on single-pixel approaches, either via structured illumination or via structured detection. Because OR-PAM is very close in its principle to fluorescence microscopy with a bucket detector, with fluorescence detection simply replaced by acoustic detection, many techniques developed for fluorescence can be adapted to photoacoustic microscopy. Structured illumination (or equivalently single-pixel) photoacoustic microscopy was first proposed by Liang et al. [8] and Yang et al. [9]: The authors adapted the principles of Fourier-encoded microscopy, where full-field illumination patterns (such as fringes [9]) are used to perform the measurement with a single-element transducer, and spatially resolved images are reconstructed from decoding the series of measurement through Fourier analysis. To our knowledge, these were the first papers to implement the so-called single-pixel imaging approach to photoacoustic microscopy. While scanning-based OR-PAM remains the most common way to perform OR-PAM [10], several groups have implemented single-pixel imaging approaches for OR-PAM in the past few years [11–15]. In this paper, we present proof-of-principle results obtained by our group by use of multiple speckle illumination in OR-PAM. We note that this approach was also implemented and published by another group [12], in parallel to our own work and first preliminary results presented at a conference in early 2017 [11]. In the context of this special issue in *Intelligent Computing*, we wrote this paper with a potentially broad readership in mind by recalling several basic principles involved in our work (photoacoustic imaging, single-pixel imaging, and reconstruction approaches) before presenting more specifically our experimental results. We first define and theoretically describe our framework for single-pixel imaging photoacoustic detection and discuss why speckle patterns are of particular interest, as compared to other types of structured illumination patterns such as fringes or Hadamard patterns, for instance. We then consider the most usual situation where the speckle illumination patterns are known via a calibration step prior to measuring a sample and introduce 3 standards and popular reconstruction methods for single-pixel imaging approaches. In particular, we consider speckle patterns produced through either optical diffusers or multimode optical fibers. We finally consider a second situation where the speckle patterns are unknown (blind structured illumination) but where a so-called memory effect can be exploited to produce calibration-free photoacoustic images, following the approach initially proposed for fluorescence imaging through thin scattering layers [16]. We illustrate all situations with results obtained with proof-of-concept experiments.

## Single-Pixel Photoacoustic Detection

We first recall the general principle of single-pixel detection, independently of the nature of the detected signals. We then discuss conditions under which a photoacoustic measurement can be described in the framework of single-pixel detection.

Image reconstruction approaches are introduced in the next sections.

## Principles of single-pixel detection

We consider an object $O(\mathbf{r})$ and an interrogation pattern $\phi_k(\mathbf{r})$. In the framework of single-pixel imaging, a set of single-pixel measurements are given by the following expression,

$$S_k = \int_{\mathbf{r}} \phi_k(\mathbf{r})O(\mathbf{r})d\mathbf{r} \tag{1}$$

where $\phi_k = \{\phi_k\}_{k=1, ..., P}$ is a set of $P$ interrogation patterns. We note that the interrogation patterns may, in practice, describe either illumination patterns or detection patterns. Different terms such as single-pixel imaging, ghost imaging, and structured illumination imaging are found in the literature, which use generally depends on communities [17]. In this work, we refer to single-pixel imaging indifferently whether the interrogation patterns are defined on the illumination path or on the detection path. In the specific case of photoacoustic imaging for which the patterns are always illumination patterns, we will also refer to single-pixel imaging. The formalism presented here is however valid for both structured illumination or structured detection, provided that the measurement is described in Eq. 1.

For some reconstruction methods, it is often useful to write Eq. 1 as a scalar product between the interrogation pattern and the object, as $S_k = \langle \phi_k, O \rangle$. In the most common case of 2D imaging, the object and interrogation patterns are 2D functions [$O(\mathbf{r}) = O(x, y)$ and $\phi_k(\mathbf{r}) = \phi_k(x, y)$], but the principle of single-pixel measurement described by the equation above is valid for any space dimension. Note that it is assumed in single-pixel imaging that $\phi_k$ does not depend in any way on the object $O$ to reconstruct [18]. In practice, objects and interrogation patterns are often spatially sampled, and the measurement can be modeled with the following equivalent discrete form:

$$S_k = \sum_{i=1}^{N} O(\mathbf{r}_i)\phi_k(\mathbf{r}_i) \tag{2}$$

For some other reconstruction algorithms, as described in further detail in the "Image reconstruction methods" section, the measurement may also be conveniently written as a linear matrix operation,

$$S = \Phi O \tag{3}$$

where $S = \{S_k\}_{k=1, ..., P}$ is the measurement vector, and $O = \{O_i\}_{i=1, ..., N} = \{O(\mathbf{r}_i)\}_{i=1, ..., N}$ is the vector that describes the object over the $N$ pixels of the sampled space. $\Phi = [\Phi_{ki}] = [\phi_k(\mathbf{r}_i)]$ is thus a $P \times N$ matrix whose rows describe each interrogation pattern.

Depending on the nature and properties of the $P$ interrogation patterns, there exist a number of methods to reconstruct the object $O(\mathbf{r}_i)$ from the measurement $S_k$ [17–19], some of which are introduced in the "Image reconstruction methods" section. Equation 1 describes the measurement process for a number of imaging methods based on the detection of electromagnetic waves, across the whole spectrum, including visible light, x-rays, terahertz waves, and infrared. It is however not limited to electromagnetic waves, and various imaging methods based on other kind of detected wave may implement single-pixel imaging, including photoacoustic imaging. Most generally, the interrogation patterns may correspond either to structured detection or structured illumination [17]. From now

on, in the context of photoacoustic imaging, we only considered the case of structured illumination. As we discuss in the next section, measurements in photoacoustic imaging may also be described in Eq. 1, under specific conditions.

## Application to photoacoustic detection

For most imaging methods based on the detection of electromagnetic waves, Eq. 1 is a direct consequence of the incoherent nature of the detected photons: In fluorescence imaging, for instance, the total detected intensity is given by the sum of the intensity emitted by each fluorophore. From that perspective, photoacoustic imaging is quite different from incoherent optical imaging techniques, as it relies on the detection of pressure signal that arise from the coherent summation of pressure fields emitted by illuminated optical absorbers. As we now demonstrate, Eq. 1 may nevertheless describe photoacoustic measurements with a single-element acoustic transducer (the acoustic "single-pixel"), provided that some conditions are met. Under the thermal confinement assumption (always verified for practical imaging application in biological tissue), the generation of photoacoustic waves $p(\mathbf{r}, t)$ is described by the following equation [20,21]:

$$\Delta p(\mathbf{r}, t) - \frac{1}{c_s^2} \frac{\partial^2 p}{\partial t^2}(\mathbf{r}, t) = -\frac{\Gamma}{c_s^2} \mu_a(\mathbf{r}) \frac{\partial \phi_r(\mathbf{r}, t)}{\partial t} \quad (4)$$

where $\phi_r(\mathbf{r}, t)$ is the local fluence rate, $\mu_a(\mathbf{r})$ is the local absorption coefficient, $\Gamma$ is the Grüneisen coefficient, and $c_s$ the constant speed of sound. Most implementations of photoacoustic imaging are based on nanosecond pulsed illumination, for which the fluence rate can be separated as $\phi_r(\mathbf{r}, t) = \phi(\mathbf{r}) f(t)$, with $\phi(\mathbf{r})$ as the local fluence (that describes the pulse energy at position $\mathbf{r}$) and $f(t)$ as a temporal pulse profile. If one considers a point-like acoustic detector, then the detected acoustic waves are filtered by the impulse response $g(t)$ of the detector. By noting $h(t) = f(t) * g(t)$ as the global impulse response, which takes into account the illumination pulse temporal profile and the tranducser response, and by use of the Green's function of the 3D wave equation, the signal $s(\mathbf{r}_d, t)$ measured by a point-like detector at positon $\mathbf{r}_d$ can be expressed as [21],

$$s(\mathbf{r}_d, t) = \frac{\Gamma}{c_s^2} \int_{\mathbf{r}} \mu_a(\mathbf{r}) \phi(\mathbf{r}) \frac{h\left(t - \frac{\|\mathbf{r}_d - \mathbf{r}\|}{c}\right)}{4\pi \|\mathbf{r}_d - \mathbf{r}\|} d\mathbf{r} \quad (5)$$

Equation 5 is similar to Eq. 1, but the integral includes an additional term that accounts for the coherent summation of pressure waves. If one now assumes that the integral is limited to a volume centered around $\mathbf{r}_0$, with size small enough such that all the photoacoustic waves arrive approximately in phase to the detector, then the detected signal can then be approximated as:

$$s(\mathbf{r}_d, t) = \frac{\Gamma}{c_s^2} \frac{h\left(t - \frac{\|\mathbf{r}_d - \mathbf{r}_0\|}{c}\right)}{4\pi \|\mathbf{r}_d - \mathbf{r}_0\|} \int_{\mathbf{r}} \mu_a(\mathbf{r}) \phi(\mathbf{r}) d\mathbf{r} \quad (6)$$

The expression above indicates that the amplitude of the detected temporal signal is exactly that given in Eq. 1, i.e., it measures the scalar product between the object to reconstruct [defined in photoacoustic imaging by $\mu_a(\mathbf{r})$] and the fluence illumination pattern. In practice, the most straightforward

single-pixel photoacoustic measurement is provided a simple peak amplitude detection. For a series of multiple illumination patterns defined by $\phi_k(\mathbf{r})$, the corresponding series of photoacoustic "single-pixel" measurement is then given by

$$S_k = s_k(\mathbf{r}_d, t_{\max}) = \frac{\Gamma}{c_s^2} \frac{h_{\max}}{4\pi \|\mathbf{r}_d - \mathbf{r}_0\|} \int_{\mathbf{r}} \mu_a(\mathbf{r}) \phi_k(\mathbf{r}) d\mathbf{r} \quad (7)$$

As discussed above, this expression is valid only if all the waves are emitted within a volume smaller than the acoustic coherence volume, i.e., the volume from which all the detected signals will be in phase. Its size depends both on the signal frequency content and the geometrical configuration of the point detector relative to the sample. Focused single-element transducers may also be used to detect the photoacoustic waves, and in this case, the detected signal may also be described approximately in Eq. 7, where the integral is limited to around the acoustic focus, with dimensions dictated by the axial and lateral resolutions. In our experimental demonstrations presented further below, we used either a focused transducer (for experiments through a diffuser) or a point-like fiber optic sensor (FOS) (for experiments through a multimode waveguide), with geometrical configuration such that all parts of the absorbing samples could be considered within the coherence volume of the detectors.

## Speckle illumination for single-pixel imaging

Measurements as described in Eq. 1 may be implemented with many different types of illumination patterns. The simplest situation occurs when the illumination patterns consist of focused optical spots scanned over the sample: In this case, the measured signal directly senses the object properties averaged over the extent of the focused spot. This is the principle of scanning microscopy, such as scanning fluorescence microscopy [22] or scanning OR-PAM [10], which provides images with a spatial resolution directly given by the size of the focused spot. The number of illumination patterns is thus generally chosen such that the spot is scanned over the whole field of view, with spatial steps typically given by the size of the spot. While this approach has the advantage of optimizing the signal-to-noise ratio and does not require any reconstruction process, 2 of its major limitations are its diffraction-limited and depth-dependent resolution and its long acquisition times (proportional to the area of the field of view). Various wide-field structured illumination techniques have been introduced in optical microscopy to palliate at least one of these limitations [23–25]. The various possible types of structured illumination patterns may be split into 2 classes, one corresponding to patterns that are straightforwardly described in simple mathematical forms, such as fringes patterns or Hadamard patterns, and the other corresponding to seemingly random (but deterministic and reproducible) patterns whose statistical properties only may be simply described mathematically, such as speckle patterns. In the context of this paper, we focus on multiple speckle illumination, whose major and key advantage is the extreme simplicity and robustness with which speckle patterns can be generated. Generating patterns of the first class not only requires sophisticated and expensive spatial light modulator (SLM) but is also potentially very sensitive to propagation from the SLM to the sample through aberration, for instance. On the contrary, as will be illustrated in the next sections, speckle patterns can be

straightforwardly generated in various situations, including propagation through optical diffusers or multimode optical fibers.

## Photoacoustic Microscopy with Known Speckle Illuminations

In this section, we consider the case for which the set of speckle patterns $\{\phi_k\}$ used to illuminate the sample is known. In experimental practice, this requires a calibration step, prior to the measurements performed on the sample. We first introduce 3 possible reconstruction methods well adapted to speckle illumination. We then present experimental results obtained in 2 different situations, one for which speckle patterns are generated through an optical diffuser and the other for which they are generated through multimode waveguides.

### Image reconstruction methods

This section recalls the principle of 3 popular reconstruction methods in the field of single-pixel imaging, which are applied on experimental photoacoustic data in the next section. Note that both the object to reconstruct and the $P$ illumination patterns are spatially sampled over $N$ pixels. We first present the 3 methods and then illustrate their behavior on a simple model case with simulated data.

#### *Correlation-based reconstruction*

Let us first consider the case of $P$ illumination patterns that form an orthonormal basis (not necessarily speckle patterns). In this case, it is required that $P = N$, and the measurement values $S_k = \langle \phi_k, O \rangle = \sum_i O(\mathbf{r}_i)\phi_k(\mathbf{r}_i)$ correspond to the coordinates of the object in the orthonormal basis. Therefore, the sampled version of the object may be straightforwardly and exactly reconstructed as,

$$O(\mathbf{r}_i) = \sum_{k=1}^{P} S_k \phi_k(\mathbf{r}_i) \tag{8}$$

This includes the cases where the illumination patterns are raster-scanned focused spot (scanning microscopy), combination of Hadamard patterns or combination of fringe patterns. When it comes to $P$ speckle illuminations patterns, which usually do not form an orthonormal set of vectors (either because $P < N$ or because of correlation between the patterns), the object may however be estimated with the following equation [26]:

$$O(\mathbf{r}_i) \propto \sum_{k=1}^{P} \left( S_k - \langle S_k \rangle \right) \left( \phi_k(\mathbf{r}_i) - \langle \phi_k(\mathbf{r}_i) \rangle \right) \tag{9}$$

Equation 9 resembles Eq. 8 but is based on the statistical properties of speckle patterns. It corresponds to a pixel-wise cross-correlation between the fluctuations of the measurement values and the fluctuations of the illumination patterns at each pixel (which are previously measured during the calibration stage). In short, it assumes that a given temporal fluctuation pattern encodes a single point in space (defined at the scale of the speckle grain). While this is the simplest possible reconstruction method, it usually requires a very large number $P$ of speckle patterns as compared to the 2 other alternative methods presented in the following sections, for equivalent image qualities and equivalent objects. Similar to the other methods, it allows to reconstruct the estimate of objects with a number $P$ of patterns that may be less than the size $N$ of the field of view and is thus a straightforward implementation of a compressed

sensing approach in the case of sparse objects. As illustrated further below, it however usually leads to images with a poor signal-to-background ratio.

#### *Pseudo-inverse approach*

The matrix formulation $S = \Phi O$ introduced in the first section indicates that reconstructing the object is equivalent to inverting a linear problem. While it is only possible in an exact manner when $P = N$ and when the set of patterns forms a basis, an estimation of the object may nevertheless always be defined as the object $\hat{O}$ that minimizes the difference between the measured values and the expected measurement $\Phi\hat{O}$:

$$\hat{O} = \underset{O}{\operatorname{argmin}} \left\{ \|S - \Phi O\|^2 \right\} \tag{10}$$

where $\|.\|$ is the L2 Euclidian norm. An exact solution to this L2-minimization problem is given by

$$\hat{O} = \Phi^+ S \tag{11}$$

where $\Phi^+$ is the Moore–Penrose pseudo-inverse. One practical way of computing $\Phi^+$ from $\Phi$ is to use its singular value decomposition $\Phi = U\Sigma V^\dagger$, which straightforwardly provides $\Phi^+ = V\Sigma^+ U^\dagger$ ($\Sigma^+$ is obtained by transposing the rectangular diagonal matrix $\Sigma$ and taking the inverse of all nonzero diagonal elements). In most software packages such as Python or MATLAB, the function pinv directly provides $\hat{O} = \text{pinv}(\Phi)S$. As for the correlation approach, the pseudo-inverse estimation can be computed for any values of $P$, including $P < N$. In addition, filtering out low singular values provides a straightforward way to perform regularization, for instance, to minimize the influence of noise on the reconstruction.

#### *Compressed sensing reconstruction*

Compressed sensing methods are powerful tools to compute solutions to underdetermined linear problems, such as $S = \Phi O$ with $P < N$, provided that there exists a basis in which $O$ have a sparse representation. In the following, we assume that $O$ is sparse in the physical space. In this case, an estimation of the object is given by [18],

$$\hat{O} = \underset{O}{\operatorname{argmin}} \left\{ \|S - \Phi O\|^2 + \lambda\|O\|_1 \right\} \tag{12}$$

where $\|.\|_1$ is the L1 norm and $\lambda$ is a regularization parameter. Note that $\lambda$ is generally tuned heuristically to optimally balance the contributions of the first term (data fidelity term) to the second term (sparsity constraint term). As opposed to the pseudo-inverse method, there is no simple computational form of the solution to Eq. 12, for which iterative minimization algorithms must be used. For all the results presented in this work, we used the same algorithm as that used by Katz et al. [19]. Note that such compressed-sensing-based reconstruction approaches have also been used in the context of AR-PAM [27–29].

#### *Illustration on simulated data*

To provide the unfamiliar reader with a feeling of the performances of each method, Fig. 1 provides a comparison of the 3 reconstructions based on the simplest possible simulated data. A binary object (PC logo) was defined over a $40 \times 40$ grid ($N = 1,600$), and $P$ random speckle patterns were generated

through Monte Carlo simulations. The intensity of all $N$ pixels followed an exponential distribution, and all patterns were linearly independent from to each other, with no correlation between pixels. The measurements were computed via Eq. 1 (with no noise). When $P = N = 1,600$, the object can be reconstructed exactly, via both the pseudo-inverse and compressed sensing approaches (Fig. 1, middle and right column). However, even when $P = N = 1,600$, the correlation-based reconstruction exhibits a substantial background fluctuation, caused by the statistical nature of the reconstruction. When $P < N$, there is no exact reconstruction possible as the set of speckle patterns is too small to form a basis. In this case, the reconstructions from the pseudo-inverse approach resemble those obtained from the correlation-based approach. On the contrary, the compressed sensing approach remains extremely accurate down to $P = N/4 = 400$, thanks to the sparsity of the object. As a take-home message from this brief illustration, the pseudo-inverse approach is the most efficient and computationally straightforward and accurate approach when $P = N$, and the compressed sensing approach may still provide very good reconstructions for $P$ much smaller than $N$ and sparse objects. The compressed sensing approach, however, requires a more complex and iterative algorithm. In practice, noise may have a substantial influence on the measured data, which both pseudo-inverse and compressed sensing approaches may minimize through a regularization parameter. A comparison of the 3 approaches on photoacoustic experimental data is shown in the next section.
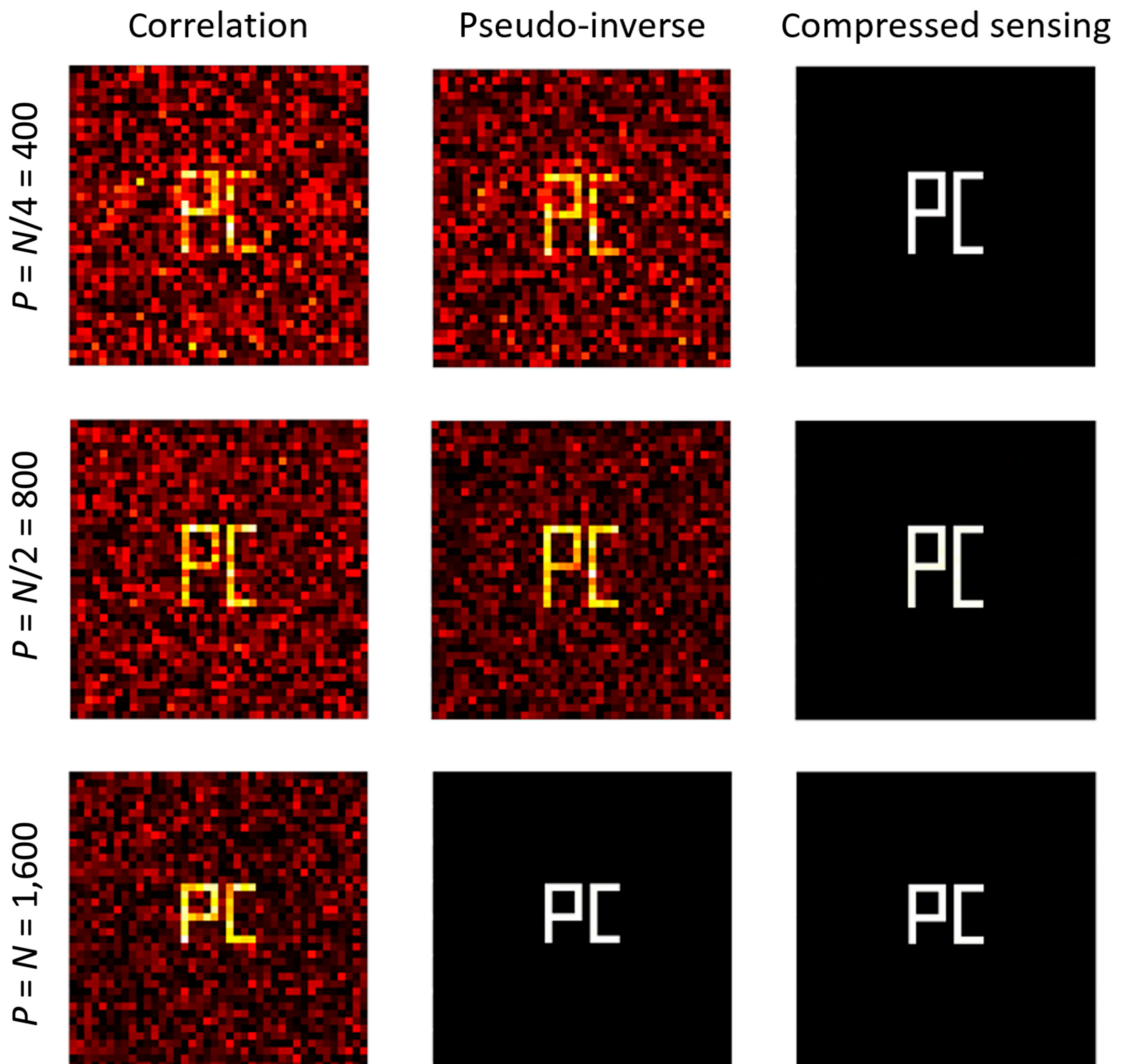


**Fig. 1.** Illustration of 3 reconstruction approaches (correlation, Moore–Penrose pseudo-inverse, and compressed sensing) on simulated data. The binary object (PC logo) is defined over a $40 \times 40$ grid ($N = 1,600$). The 3 lines correspond to the number $P$ of speckle patterns used to reconstruct the object with each method.
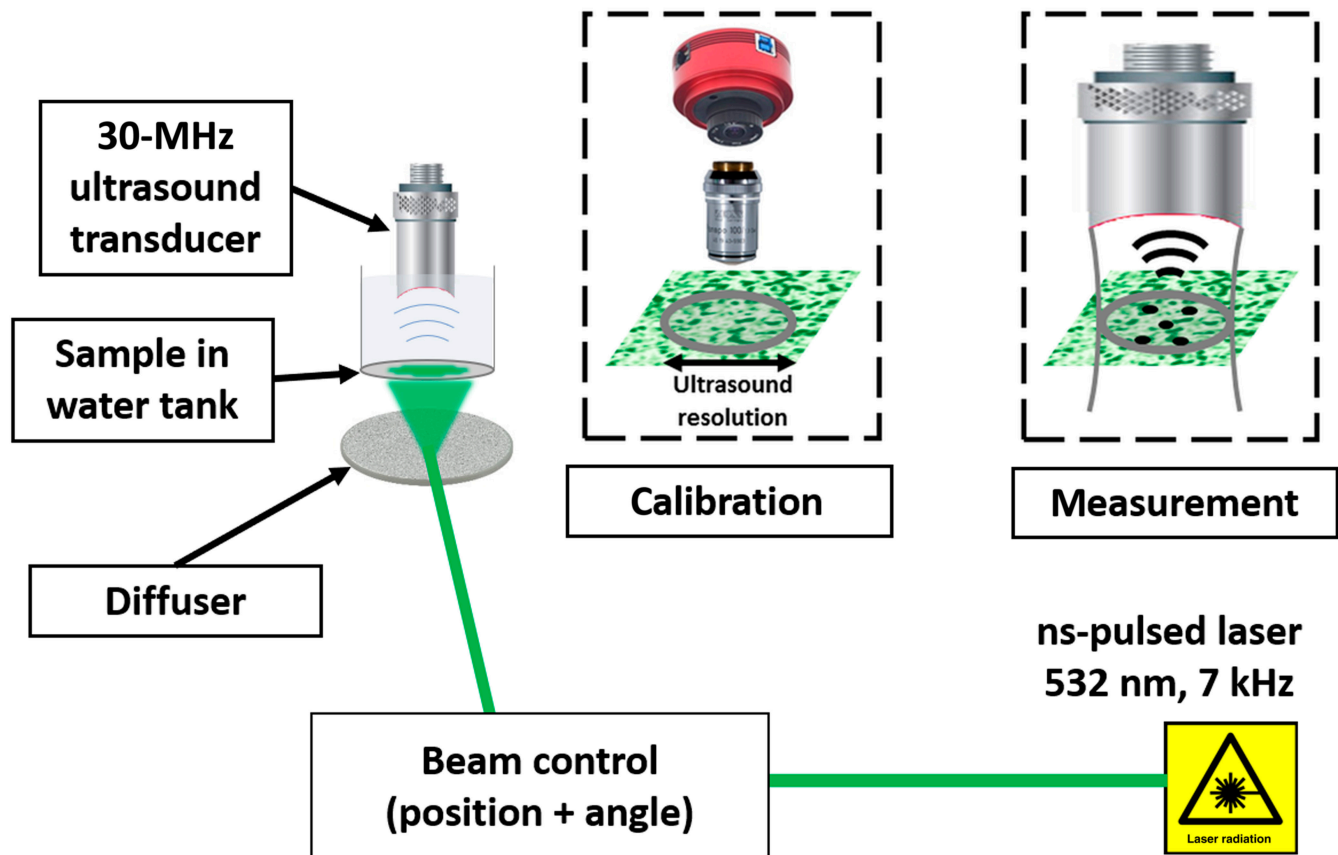
**Fig. 2.** Schematic of the experimental setup used to perform imaging photoacoustic microscopy through a diffuser. The sample is held horizontal in a water tank and is illuminated by speckle patterns generated through a ground glass diffuser. The diffuser is illuminated by a coherent laser beam, and various speckle realizations are obtained by changing the beam positions and incidence on the diffuser. Speckle patterns in the sample plane are first measured with a CCD camera as a calibration step before the camera is replaced by a focused ultrasound transducer for the measurement step.

## Photoacoustic microscopy through a diffuser

In this section, we present experimental results obtained with speckle patterns generated through a ground glass diffuser and photoacoustic signals detected with a focused ultrasound transducer.

### *Experimental setup*

A schematic representation of the experimental setup is shown in Fig. 2. The samples used consisted of 2D optically absorbing patterns, printed with a high-resolution photoplotter (Selba, Switzerland) on a transparent polymer substrate (thickness of 175 µm; Fujifilm HG New HPR-7S). The samples were placed in a water-filled microdish on top of a microscope glass coverslip. The samples were illuminated from the bottom by speckle patterns generated through a ground glass diffuser (Thorlabs DG10-220). The laser light was generated using a single-longitudinal-mode pulsed laser at 532 nm, 5-ns pulse duration, 7-kHz pulse repetition rate, and 60 µJ per pulse (Cobolt Thor Series). Combinations of lenses and galvanometric mirrors were used to control the position and incidence angle of the collimated beam onto the diffuser. In practice, the position of the beam on the diffuser was kept constant, while both the inclination and azimuthal angles were varied to generate different speckle patterns on the sample. The diameter of the beam on the diffuser was tuned such that the speckle grain size in the sample plane was approximately 5 µm.
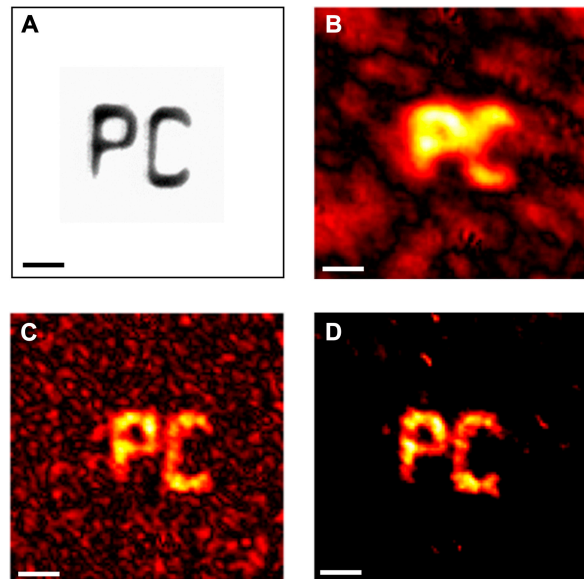


**Fig. 3.** Illustration of 3 reconstruction approaches on the same experimental data. The absorbing sample (PC logo; photograph shown in A) was illuminated with $P = 1{,}600$ speckle patterns, which approximately corresponds the number of speckle grain within the reconstructed total field of view ($N = 200 \times 200 = 40{,}000$ camera pixels). (B) Correlation-based reconstruction. (C) Pseudo-inverse reconstruction. (D) Compressed sensing reconstruction. Only part of the reconstructed field of view centered on the object is shown. Scale bars, 20 µm.
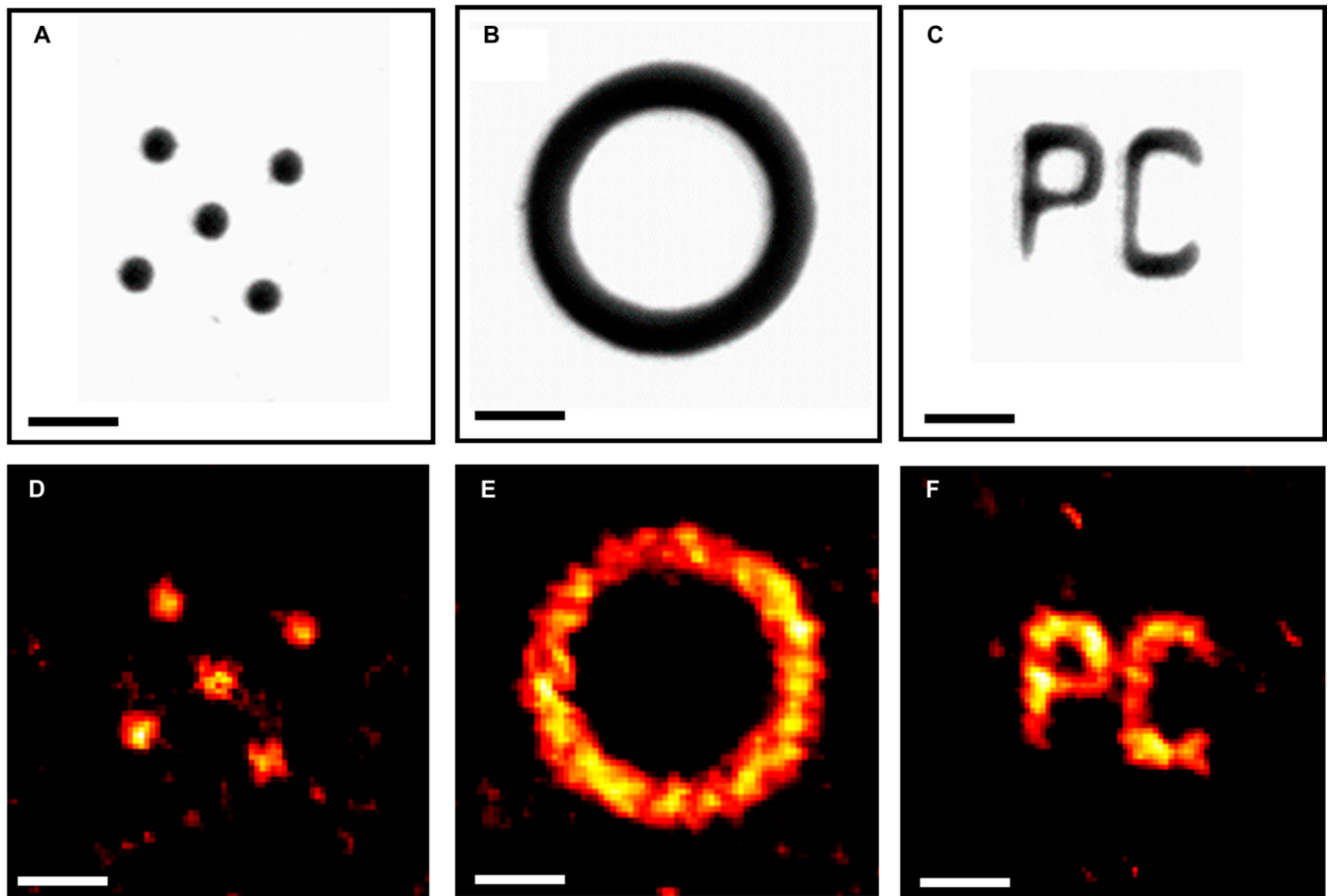
**Fig. 4.** (A to C) Photographs of the 3 absorbing samples obtained with a conventional transmission microscope. (D to F) Corresponding objects reconstructed with the compressed sensing approach, from $P=1,600$ speckle patterns, which approximately corresponds the number of speckle grain within the reconstructed field of view ($N=200\times200=40,000$ camera pixels). Only part of the reconstructed field of view centered on the object is shown. Scale bars, 25 μm.

The speckle patterns were measured during a calibration step (without the sample and without the ultrasound transducer) with a charge-coupled device (CCD) camera. Photoacoustic signals were detected with a single-element focused ultrasound transducer (Sonaxis HFM2; central frequency of 34 MHz, focal length of 12.4 mm) connected to a digital oscilloscope through a preamplifier. The single-pixel measurement was defined as the peak amplitude of the ultrasound signal. The dimension of the reconstructed field of view was 200 μm × 200 μm, which corresponded to approximately $40 \times 40 = 1,600$ speckle grains and a number $N = 200 \times 200 = 40,000$ camera pixels. For this first proof of principle, photoacoustic signals were averaged over 1,000 laser shots for each speckle pattern in order to minimize the influence of the measurement noise on the reconstruction.

### Results

Figure 3 illustrates the images obtained by each of the 3 reconstruction approaches introduced earlier for the exact same set of data. As expected, the best reconstruction is obtained for the compressed sensing approach: Both the correlation- and pseudo-inverse-based reconstruction exhibit a strong fluctuating background. We note that the pseudo-inverse and the compressed sensing approach both provide an enhancement resolution as compared to the correlation approach. Both approaches take into account the known speckle patterns and can be seen as

deconvolution methods, for which the resolution is dictated by the highest spatial frequency content of the speckle pattern, whereas the resolution of the correlation approach is given by the average speckle size. Figure 4 further illustrates images obtained with the compressed sensing approach for 3 different samples. The results shown in Figs. 3 and 4, adapted from preliminary results presented at a conference [11], demonstrated for the first time to our knowledge that speckle patterns could be used to perform OR-PAM. Because the speckle patterns need to be known via a calibration step, this method is obviously not adapted to image inside a scattering sample. However, it offers an inexpensive and flexible means to perform photoacoustic microscopy with no focusing optics, by means of a simple off-the-shelf diffuser, following the exact same strategy as that developed for purely optical approaches [30,31].

## Photoacoustic microendoscopy through multimode fibers

Beyond the proof-of-concept demonstration presented in the previous section, exploiting speckle illumination to perform optical-resolution imaging finds an interesting application in the context of microendoscopy through multimode fibers (MMFs). Optical imaging through MMFs has been the topic of extensive research efforts over the past decade [32–36], as it

provides a means to design minimally invasive endoscope, as compared to more conventional approaches based on bundles of single-mode fiber. However, MMFs scramble the light during the propagation from the proximal (input) facet of the fiber to its distal (sample) facet, and there is no straightforward way to
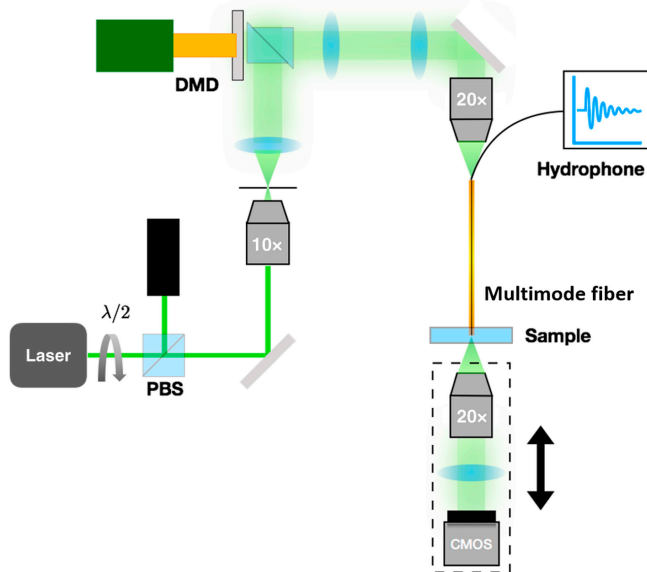


**Fig. 5.** Schematic of the experimental setup used to perform photoacoustic microendoscopy through a multimode waveguide. Various speckle patterns were produced at the output (sample side) of the multimode waveguide using a binary amplitude light modulator (DMD, digital micromirror device) that controls the input illumination. PBS, polarizing beam splitter. The CMOS (complementary metal–oxide semiconductor) camera is used only for the calibration steps to measure the speckle patterns in the sample plane. The photoacoustic signals are measured with a fiber optic hydrophone attached next to the waveguide.
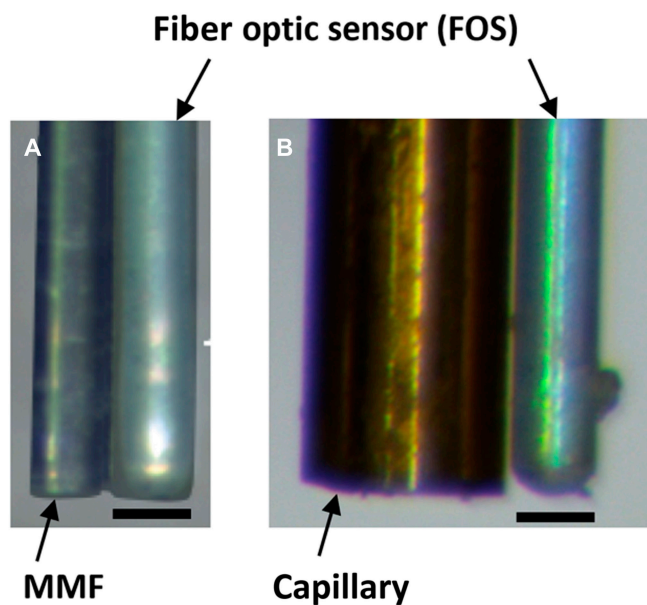


**Fig. 6.** (A) Side-view photograph of a lensless imaging tip composed of a circular multimode fiber (MMF) with a fiber optic sensor (FOS) aside. (B) Side-view photograph of a lensless imaging tip composed of a capillary with a FOS aside. The speckle illumination patterns are created by multimode-guided propagation through either the MMF or the capillary walls, and the photoacoustic signal is measured by FOS. The sensitive area of the FOS is only 10 μm in diameter. Scale bars, 125 μm.

image through MMFs. Complex wavefront shaping provides a means to deal with multimode propagation and, for instance, focus light at the distal end. Focusing through MMF for imaging was first demonstrated for fluorescence microendoscopy [35] and later adapted to photoacoustic microendoscopy [37,38]. However, imaging is also possible by exploiting the speckle patterns that are naturally produced at the output of MMFs for almost any input patterns. The idea that imaging could be performed through MMFs with speckle illumination and single-pixel detection was first introduced in the 1990s in a pioneer work by Bolshtyansky and Zel'dovich [39]. The topic has then become very active in the last decade, with an emphasis on the compressed sensing capabilities provided by speckle patterns at the output of a multimode waveguide [40–43]. Here, we present results obtained by adapting the approach initially developed for fluorescence microscopy to photoacoustic microendoscopy.

### Experimental setup

To obtain the results presented in this work, we used the setup shown in Fig. 5, which is the same as that used for our first preliminary experiments of photoacoustic microendoscopy with speckle illumination [13]. It is further described in more detail in a later publication in which we demonstrated that both fluorescence and photoacoustic microendoscopy can be performed simultaneously with the same setup [44]. A major novelty of our approach, as compared as purely optical methods, is based on the detection of photoacoustic waves directly at the imaging tip of the MMF by adding a FOS next to the MMF. We present results obtained with 2 types of multimode waveguides, a conventional circular step-index MMF and a microcapillary waveguide. In both cases, we used a custom highly sensitive
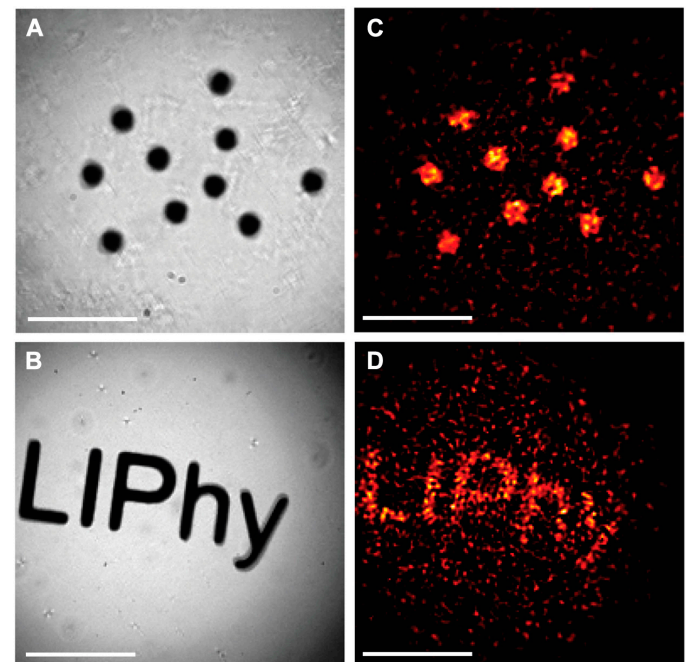


**Fig. 7.** (A and B) Photographs of the 2 absorbing patterns placed at the distal facet of a step-index MMF, obtained with a conventional transmission microscope. (C and D) Corresponding photoacoustic images obtained by the compressed-sensing-based reconstruction approach applied to photoacoustic signals measured by a FOS attached next to the MMF. Scale bars, 50 μm.
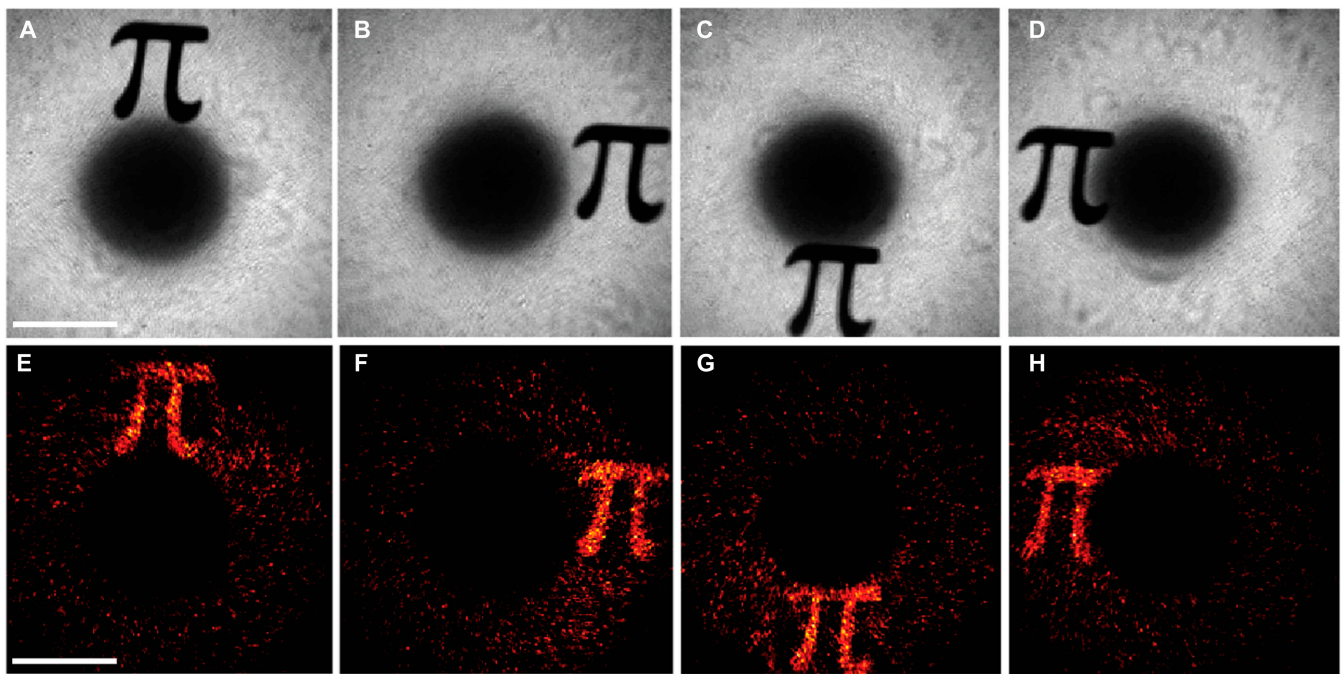
**Fig. 8.** (A to D) Photographs of the absorbing pattern (letter π) positioned at different locations at the distal tip of a microcapillary waveguide, obtained with a conventional transmission microscope. The dark central zone corresponds to the inside of the capillary, as light is guided only through the glass wall (bright zone). (E to H) Corresponding photoacoustic images obtained by the compressed-sensing-based reconstruction approach, applied to photoacoustic signals measured by a FOS attached next to the capillary. Scale bars, 100 μm.

FOS, developed at University College London. A detailed description of the sensor and its working principle may be found in [45]. As compared to our first preliminary results [13], which were obtained with a commercial FOS and required thousands of averaging in order to reach appropriate signal-to-noise ratio, the results presented in the next sections were obtained with no more than 100 laser shots per speckle pattern. The FOS is only 125 μm in diameter, such that the whole system remains minimally invasive, as illustrated in Fig. 6B. Note that the active area of the FOS is only 10 μm in diameter, and the detector can thus be considered as a point-like detector.

### Results through a conventional circular MMF
Figure 7 shows 2 samples and their photoacoustic images obtained through a conventional circular step-index MMF (Thorlabs DCF13; 105-μm core/125-μm cladding), reconstructed with the compressed sensing approach. Four thousand speckle patterns (previously measured through a calibration step) were used to illuminate the samples. We note that the shape of the fiber must remain the same between the calibration and the imaging acquisition such that the illumination patterns do not vary. Reconstruction was computed over a field of view of $200 \times 200$ pixel, and 100 shots were used per speckle pattern to increase the signal-to-noise ratio via coherent averaging. As illustrated in Fig. 7, various types of objects (bead-like or more continuous patterns such as letters) could be imaged throughout the whole core of the MMF.

### Results through a capillary waveguide
As introduced in some of our earlier works [46,47], microcapillaries have very interesting waveguide properties, which make them of interest for the design of minimally invasive probes.

Both their glass walls and their inner hole may behave as waveguides for different types of waves. In our first investigation of microcapillaries for photoacoustic sensing [46], we experimentally demonstrated that when filled with water, the inner fluid core can guide photoacoustic waves from the distal (sample) side to a transducer located at the proximal (detector) side. Viscous acoustic losses however limited the practical length of the device to a few centimeters. We then further demonstrated that it was possible to implement complex wavefront shaping of light guided through the glass part of the capillary to perform either fluorescence or photoacoustic scanning microscopy through the capillary [47]. For photoacoustic imaging, not only did the approach required wavefront shaping to focus light through the device (as for fluorescence) but also the detection of the photoacoustic waves was performed with a bulky single-element transducer, incompatible in practice with a minimally invasive device. Here, by using a FOS, we demonstrate that it is possible to perform minimally invasive photoacoustic micro-endoscopy with a microcapillary and an all-optical approach. The inner core may be used either to insert the FOS inside the capillary or, if the FOS is attached next to the capillary, to provide additional functionalities to the microendoscope such as a microfluidic access to the sample or the addition of an electrode for electrophysiology recording. Figure 8 shows results obtained through a capillary waveguide with the FOS attached next to it, as illustrated on Fig. 6B. In this case, the field of view has the same geometry as the capillary cross section because the light is only guided through the glass walls. Although the FOS was attached to the side of the capillary, Fig. 8 shows that objects located a few hundred microns away from the capillary facet could be reconstructed over the whole circumference of the capillary.

# Photoacoustic Microscopy with the Optical Memory Effect

In this last section, we consider the case for which the speckle patterns are unknown, a situation commonly referred to as blind structured illumination. We first recall the principle of imaging with blind structured illumination thanks to the optical memory effect, which was introduced in a pioneer work by Bertolotti et al. [16] for fluorescence imaging. We then show experimental results obtained by following the exact same approach for photoacoustic microscopy measurements.

## Imaging with unknown speckle patterns via the memory effect
### Principle of the measurements
We consider $\phi_k(\mathbf{r}, \boldsymbol{\alpha})$ the intensity pattern in the sample plane, now depending one some given experimental parameter $\boldsymbol{\alpha}$. In the context of this work, $\boldsymbol{\alpha} = (\alpha_x, \alpha_y)$ describes the direction of incidence of a collimated beam onto the diffuser that creates the speckle pattern in the sample plane. We now show that even if the speckle patterns $\phi_k(\mathbf{r}, \boldsymbol{\alpha})$ are unknown, it nonetheless remains possible to find relationships between statistical properties of the measurement and properties of the object. To do so, we define the following normalized statistical cross-correlation functions:

$$C_\phi(\mathbf{r}, \mathbf{r}', \boldsymbol{\alpha}, \boldsymbol{\alpha}') = \left\langle \widehat{\phi}_k(\mathbf{r}, \boldsymbol{\alpha}) \widehat{\phi}_k(\mathbf{r}', \boldsymbol{\alpha}') \right\rangle \qquad (13\text{A})$$

$$C_S(\boldsymbol{\alpha}, \boldsymbol{\alpha}') = \left\langle \widehat{S}_k(\boldsymbol{\alpha}) \widehat{S}_k(\boldsymbol{\alpha}') \right\rangle \qquad (13\text{B})$$

where $\langle \cdot \rangle$ denotes ensemble averaging over speckle realizations. In the definitions above, $S_k(\boldsymbol{\alpha}) = \int_\mathbf{r} O(\mathbf{r}) \phi_k(\mathbf{r}, \boldsymbol{\alpha}) \mathrm{d}\mathbf{r}$ is the measurement associated with the $k$th realization of the illumination pattern with parameter $\boldsymbol{\alpha}$, and $\widehat{x_k} = \frac{x_k - \langle x_k \rangle}{\sqrt{\langle x_k^2 - \langle x_k \rangle^2 \rangle}}$ is defined as the standardized centered random variable associated to any random variable $x_k$ ($\phi_k$ and $S_k$ in Eqs. 13A and 13B). The statistical correlation between the signals $S_k$ is defined explicitly as,

$$\left\langle S_k(\boldsymbol{\alpha}) S_k(\boldsymbol{\alpha}') \right\rangle = \left\langle \int_\mathbf{r} O(\mathbf{r}) \phi_k(\mathbf{r}, \boldsymbol{\alpha}) \mathrm{d}\mathbf{r} \int_{\mathbf{r}'} O(\mathbf{r}') \phi_k(\mathbf{r}', \boldsymbol{\alpha}') \mathrm{d}\mathbf{r}' \right\rangle$$

$$= \iint_{\mathbf{r}', \mathbf{r}} O(\mathbf{r}) O(\mathbf{r}') \left\langle \phi_k(\mathbf{r}, \boldsymbol{\alpha}) \phi_k(\mathbf{r}', \boldsymbol{\alpha}') \right\rangle \mathrm{d}\mathbf{r} \mathrm{d}\mathbf{r}'$$

By introducing the standardized centered variables $\widehat{S}_k$ and $\widehat{\phi}_k$ and assuming that $\phi_k$ represents stationary (i.e., mean and variance are constant over $\mathbf{r}$ and $\boldsymbol{\alpha}$) and fully developed speckle intensity patterns (i.e., $\sqrt{\langle \phi_k \rangle^2 - \langle \phi_k \rangle^2} = \langle \phi_k \rangle$), tedious but simple calculations lead to the following explicit expression equivalent to Eq. 13B:

$$C_S(\boldsymbol{\alpha}, \boldsymbol{\alpha}') = \frac{1}{K^2} \frac{\iint_{\mathbf{r}, \mathbf{r}} O(\mathbf{r}) O(\mathbf{r}') C_\phi(r, r', \boldsymbol{\alpha}, \boldsymbol{\alpha}') \mathrm{d}\mathbf{r} \mathrm{d}\mathbf{r}'}{\left[ \int_\mathbf{r} O(\mathbf{r}) \mathrm{d}\mathbf{r} \right]^2} \qquad (14)$$

where $K = \frac{\sqrt{\langle S_k \rangle^2 - \langle S_k \rangle^2}}{\langle S_k \rangle}$ corresponds to the contrast of the measured signal. In the most general case where the speckle patterns $\widehat{\phi}_k(\mathbf{r}, \boldsymbol{\alpha})$ and $\widehat{\phi}_k(\mathbf{r}', \boldsymbol{\alpha}')$ are uncorrelated, both $C_\phi = 0$ and $C_S = 0$ for $\boldsymbol{\alpha} \neq \boldsymbol{\alpha}'$ and the equation above carries no information on the object $O(\mathbf{r})$. Here, we consider that the speckle patterns produced by illuminating the sample through a thin diffuser exhibits a shift memory effect in the sample plane when the laser beam is tilted onto the diffuser. In this case, under the classical assumption that speckle patterns are second-order stationary random process, the memory effect is described analytically through the following tilt–shift relationship:

$$C_\phi(\mathbf{r}, \mathbf{r}', \boldsymbol{\alpha}, \boldsymbol{\alpha}') = c_\phi(\| \Delta r - \Delta \boldsymbol{\alpha} F \|) g(\Delta \boldsymbol{\alpha}) \qquad (15)$$

where $F$ is the distance between the object plane and the diffuser, $c_\phi(\| \Delta \mathbf{r} \|) = \left\langle \widehat{\phi}_k(\mathbf{r} + \Delta \mathbf{r}) \times \widehat{\phi}_k(\mathbf{r}) \right\rangle$ is the space-invariant autocorrelation of a speckle intensity pattern, and $g(\Delta \boldsymbol{\alpha})$ is a function peaked around zero that describes the range of the memory effect ($g = 1$ for a perfect memory effect). Finally, by a change of variables in Eq. 14, one finally gets the following expression for the statistical cross-correlation function of the measurement:

$$C_S(\Delta \boldsymbol{\alpha}) = K^{-2} g(\Delta \boldsymbol{\alpha}) \int_\mathbf{r} C_O(\mathbf{r}) C_\phi(\mathbf{r} - \Delta \boldsymbol{\alpha} F) \mathrm{d}\mathbf{r}$$

$$= K^{-2} g(\Delta \boldsymbol{\alpha}) \left[ C_O{}^* C_\phi \right] (\Delta \boldsymbol{\alpha} F) \qquad (16)$$

Equation 16 states that thanks to the optical memory effect, the statistical cross-correlation function of measurements obtained for various incidence angles (as defined by $\boldsymbol{\alpha}$) is equal to the normalized spatial autocorrelation of the object $C_O$ convolved with the statistical autocorrelation of a speckle intensity pattern $C_\Phi$, weighted by the range of the memory effect. This result was first given and exploited by Bertolotti et al. [16] to perform fluorescence imaging through a diffuser: Because the autocorrelation function of a speckle pattern is a peaked function with a width given by the size of a speckle grain, the autocorrelation of the measurements is directly a measurement of the autocorrelation of the object, with the resolution of the speckle grain and a range limited by the memory effect. In practice, a robust statistical estimation of $C_S(\Delta \boldsymbol{\alpha})$ often requires both ensemble averaging over speckle realization and averaging over measurements for a given value of $C_S(\Delta \boldsymbol{\alpha})$ (i.e., computing a spatial correlation of the measurements for a given speckle realization) thanks to ergodicity.

### Image reconstruction
As introduced in the previous section, the statistical correlation of the measurements obtained for various incidence angles provides an estimation of the spatial autocorrelation function of the object. To reconstruct the object, it is thus necessary to invert the spatial autocorrelation. From the Fourier convolution theorem, the knowledge of the autocorrelation of an object yields the modulus of its Fourier transform, which is not enough to retrieve the object itself, as the phase of its Fourier transform is missing. Nevertheless, it is possible to numerically invert the autocorrelation and estimate the object by setting constraints such as the object is positive and/or real-valued and run iterative phase retrieval algorithms [16,48]. For both
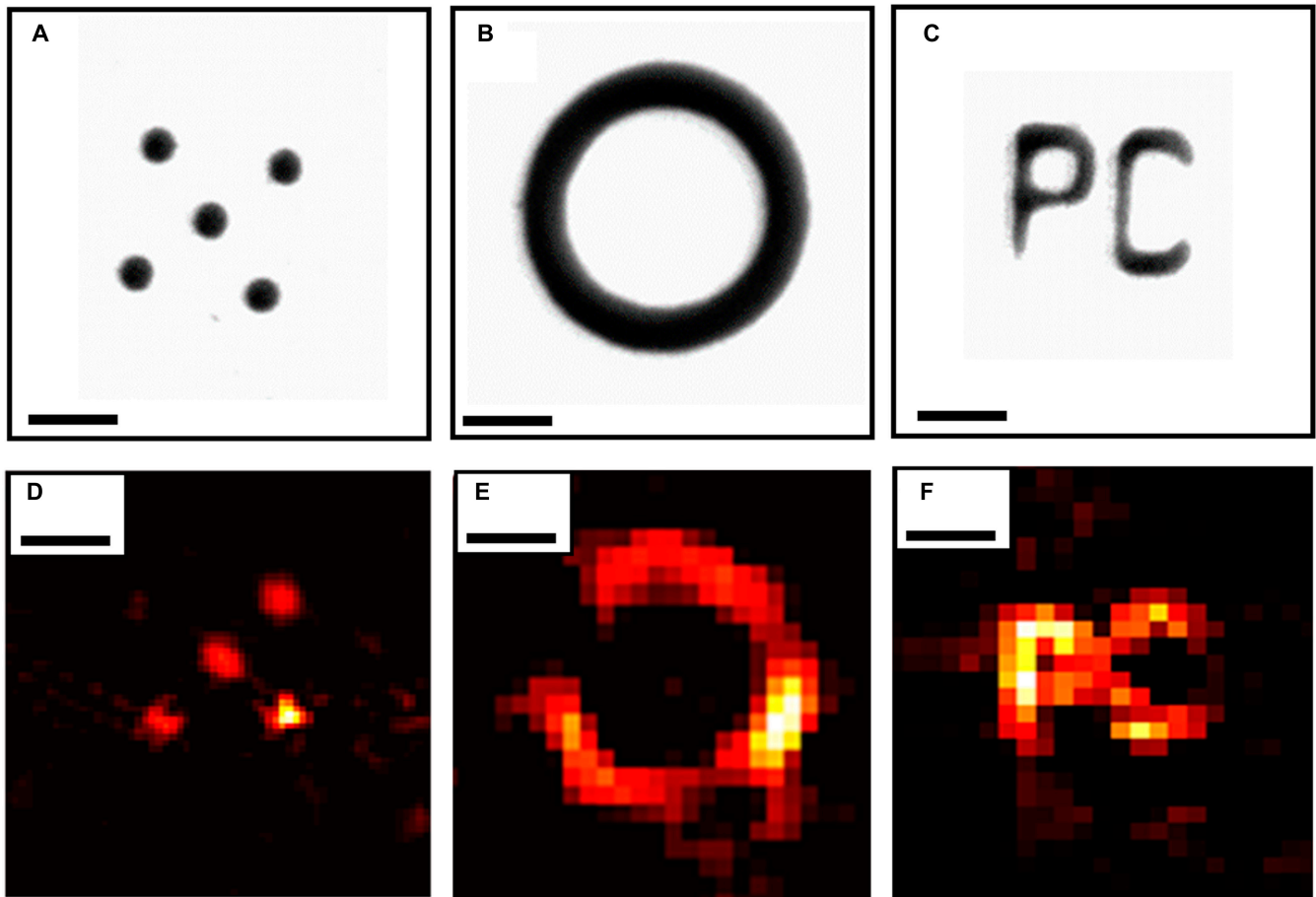
**Fig. 9.** (A to C) Photographs of the 3 absorbing samples obtained with a conventional transmission microscope. (D to F) Corresponding objects reconstructed from the photoacoustic measurements obtained by scanning unknown speckle patterns over the sample hidden behind a diffuser, with use of the optical memory effect. Scale bars, 25 μm.

fluorescence microscopy and photoacoustic microscopy, the target to reconstruct is the absorption coefficient, which is both real and positive: To obtain the experimental results presented in the next section, we followed Bertolotti et al. [16] and used a modified version of the Gerchberg–Saxton proposed by Fienup [48] in a seminal paper published in the late 1970s.

### Experimental validation through a thin scattering layer

To demonstrate blind structured illumination photoacoustic microscopy through a thin diffuser with the memory effect, we used the exact same setup as shown in Fig. 2. Galvanometric mirrors coupled to 4-f systems (not shown in the figure) were used to vary the beam incidence angle onto the diffuser while keeping the same beam position and to scan a given speckle pattern over the diffuser thanks to the memory effect. With the thin diffuser used, the memory effect in the sample plane extended over several hundred microns, much larger than the size of the objects to reconstruct, and its finite range was thus neglected in the reconstruction ($g(\alpha) = 1$). Figure 9 shows the results obtained for 3 different types of objects. Statistical cross-correlations were estimated by averaging over 13 (sample a), 5 (sample b), and 8 (sample c) speckle realizations and by averaging over space thanks to ergodicity. Speckle patterns were scanned with a step of 4 μm in the sample plane, with scan dimensions 41 × 41 (sample a), 51 × 51 (sample b), and 51 × 51

(sample c), although all reconstructions are shown with the same field of view. The photoacoustic images shown in Fig. 9 are, to our knowledge, the first photoacoustic microscopy images obtained through a diffusing medium with a blind structured illumination. A scanning approach with a speckle pattern was also mentioned by Meiri et al. [12], but the speckle pattern has to be known, and this approach is in the end equivalent to multiple speckle illumination with known patterns.

### Discussion

In this paper, we recalled the general principle of single-pixel imaging with structured illumination, which we applied in this work to photoacoustic imaging. From single-pixel photoacoustic measurements, obtained for multiple speckle illumination, images of absorbing samples are reconstructed through various possible reconstructions. The common link between the different experiments presented here is the possibility to straightforwardly generate speckle illuminations in a controlled and reproducible way, either with a diffuser or an MMF. This fine control in combination with compressed sensing methods allows to reconstruct the image with the resolution given by the size of the optical speckle grain, which is the same as the size of a focal spot created through an equivalent numerical aperture. The major limitation of approaches based on multiple speckle illumination, common to other types of wide-field structured illumination patterns

and shared by different detection modalities such as fluorescence and photoacoustics, is related to the fluctuation-to-noise ratio: the information on the object to reconstruct is contained within the signal fluctuations, rather than the signal amplitude itself. Large objects, as compared to the characteristic size of the illumination pattern (i.e., the size of the speckle grain for speckle illumination), lead to small values of the fluctuation-to-signal ratio. The ability to measure speckle-induced fluctuations on top of noise fluctuations thus depends on both the signal-to-noise ratio and the available dynamic range. From this perspective, methods based on raster scanning of focal spot are generally much more efficient as compared to structured illumination.

In the context of photoacoustic microscopy, we recently demonstrated that the highly sensitive FOS developed at University College London [45] enabled single-shot photoacoustic microscopy through an MMF by scanning a spot with complex wavefront shaping [38]. In the results present here, the same FOS required averaging over typically a hundred shots to get images of similar quality via multiple speckle illumination. From the perspective of the total measurement time (which dictates the imaging frame rate), multiple speckle illumination may require orders of magnitude less patterns than raster scan approaches, provided that the sample to image is very sparse. The number of random patterns (and consequently the measurement time) depends strongly on the number of nonzero pixels in the object, whereas it is directly proportional to the field of view and independent from the sample for raster scan approaches. Moreover, the sparsest the sample, the higher the fluctuation-to-noise ratio, which is also a key parameter as the total acquisition time will depend not only on the number of patterns but also on the number of averages per illumination pattern. In the experiments presented in Figs. 7 and 8, we used about 10 times less speckle patterns than pixels in the image (4,000 patterns versus $200 \times 200$ pixels), but because of the limited fluctuation-to-noise ratio, we had to average about 100 times. In this case, the advantage of the approach was, thus, not the total acquisition time, which was 10 times larger the equivalent acquisition time for a raster scan approach, but rather its simplicity: Raster scanning a focal spot would have required a rather involved calibration to be able to create and scan a focal spot, while calibrating only the speckle intensity pattern was straightforward. Additionally, in biomedical photoacoustic imaging, which uses pulsed laser, it is important to stay below the maximum permissible exposure for tissue, and therefore, spreading the illumination into speckle patterns instead of creating a strong bright focal point can be important to reduce the thermal damage. For very sparse samples, multiple speckle illumination is expected to be also beneficial in terms of total acquisition time, but this was not demonstrated here.

In the end, the choice between a multiple speckle illumination approach and a more conventional scanning approach will depend on several considerations, including trade-offs between instrumental complexity (usually for wavefront-shaping-based approaches) and reconstruction complexity (for compressed-sensing approach with structured illumination) and between signal-to-noise performances (higher for scanning based approach) and acquisition time (potentially shorter for structured illumination and sparse sample).

The results presented in this work illustrate how photoacoustic microscopy can harness many of the structured illumination methods developed initially for pure optical methods such as fluorescence microscopy simply by replacing light detection with acoustic detection. As a consequence, multimodality approaches may be implemented with the same illumination scheme, as we demonstrated with hybrid fluorescence and photoacoustic microscopy with multiple speckle illumination [44]. As a major drawback for wide-field-structured illumination approach, the sensitivity of photoacoustic detection remains relatively low as compared to fluorescence sensing, but we hope that the development of more and more sensitive detectors [45,49,50] will enable biomedical applications of single-pixel photoacoustic microscopy in the near future.

## Data Availability

All data needed to evaluate the conclusions in this paper are present in the manuscript. Additional data related to this paper may be requested from the authors.

## References

1. Bell AG. Art. XXXIV.—On the production and reproduction of sound by light. *Am J Sci*. 1880;20(118):305–324.
2. Manohar S, Razansky D. Photoacoustics: A historical review. *Adv Opt Photon*. 2016;8:586–617.
3. Wang LV, Hu S. Photoacoustic tomography: In vivo imaging from organelles to organs. *Science*. 2012;335(6075):1458–1462.
4. Beard P. Biomedical photoacoustic imaging. *Interface focus*. 2011;1(4):602–631.
5. Deán-Ben X, Gottschalk S, Mc Larney B, Shoham S, Razansky D. Advanced optoacoustic methods for multiscale imaging of in vivo dynamics. *Chem Soc Rev*. 2017;46(8):2158–2198.
6. Das D, Sharma A, Rajendran P, Pramanik M. Another decade of photoacoustic imaging. *Phys Med Biol*. 2021;66(5):05TR01.

7. Yao J, Wang LV. Photoacoustic microscopy. *Laser Photonics Rev*. 2013;7(5):758–778.

8. Liang J, Gao L, Li C, Wang LV. Spatially fourier-encoded photoacoustic microscopy using a digital micromirror device. *Opt Lett*. 2014;39(3):430–433.

9. Yang J, Gong L, Xu X, Hai P, Shen Y, Suzuki Y, Wang LV. Motionless volumetric photoacoustic microscopy with spatially invariant resolution. *Nat Commun*. 2017;8(1):780.

10. Jeon S, Kim J, Lee D, Baik JW, Kim C. Review on practical photoacoustic microscopy. *Photoacoustics*. 2019;15:Article 100141.

11. Poisson F, Stasio N, Moser C, Psaltis D, Bossy E. Multiple speckle illumination for optical-resolution photoacoustic imaging. Paper presented at: SPIE BiOS 10064. Proceedings of the Photons Plus Ultrasound: Imaging and Sensing 2017; 2017 Jan 28–Feb 2; San Francisco, CA.

12. Meiri A, Strohm EM, Kolios MC, Zalevsky Z. Spatial interference encoding patterns based photoacoustic microscopy. *Opt Commun*. 2017;401:23–28.

13. Caravaca-Aguirre AM, Poisson F, Bossy E. Speckle based optical-resolution photoacoustic endoscopy (conference presentation). Paper presented at: SPIE BiOS 10494. Proceedings of the Photons Plus Ultrasound: Imaging and Sensing 2018; 2018 Jan 27–Feb 1; San Francisco, CA.

14. Amjadian M, Mostafavi SM, Kavehvash Z, Faez R. Fast three-dimensional super-resolution photoacoustic microscopy imaging. *Opt Eng*. 2021;60(12):Article 123108.

15. Torke PR, Nuster R, Paltauf G. Photoacoustic computational ghost imaging. *Opt Lett*. 2022;47(6):1462–1465.

16. Bertolotti J, van Putten EG, Blum C, Lagendijk A, Vos WL, Mosk AP. Non-invasive imaging through opaque scattering layers. *Nature*. 2012;491(7423):232–234.

17. Gibson GM, Johnson SD, Padgett MJ. Single-pixel imaging 12 years on: A review. *Opt Express*. 2020;28(19):28190–28208.

18. Duarte MF, Davenport MA, Takhar D, Laska JN, Sun T, Kelly KF, Baraniuk RG. Single-pixel imaging via compressive sampling. *IEEE Signal Process Mag*. 2008;25(2):83–91.

19. Katz O, Bromberg Y, Silberberg Y. Compressive ghost imaging. *Appl Phys Lett*. 2009;95(13):Article 131110.

20. Diebold G, Sun T, Khan M. Photoacoustic monopole radiation in one, two, and three dimensions. *Phys Rev Lett*. 1991;67(24):3384–3387.

21. Wang LV, Wu H-i. *Biomedical optics: Principles and imaging*. Hoboken (NJ): John Wiley & Sons; 2012.

22. Wilson T, Sheppard C. *Theory and practice of scanning optical microscopy*. London (UK): Academic Press London; 1984. vol. 180.

23. Neil MA, Juškaitis R, Wilson T. Method of obtaining optical sectioning by using structured light in a conventional microscope. *Opt Lett*. 1997;22(24):1905–1907.

24. Saxena M, Eluru G, Gorthi SS. Structured illumination microscopy. *Adv Opt Photon*. 2015;7(2):241–275.

25. Heintzmann R, Huser T. Super-resolution structured illumination microscopy. *Chem Rev*. 2017;117(23):13890–13908.

26. Akhlaghi MI, Dogariu A. Compressive correlation imaging with random illumination. *Opt Lett*. 2015;40(19):4464–4467.

27. Han Y, Ding L, Ben XLD, Razansky D, Prakash J, Ntziachristos V. Three-dimensional optoacoustic reconstruction using fast sparse representation. *Opt Lett*. 2017;42(5):979–982.

28. Egolf DM, Chee RK, Zemp RJ. Sparsity-based reconstruction for super-resolved limited-view photoacoustic computed tomography deep in a scattering medium. *Opt Lett*. 2018;43(10):2221–2224.

29. Vilov S, Arnal B, Hojman E, Eldar YC, Katz O, Bossy E. Super-resolution photoacoustic and ultrasound imaging with sparse arrays. *Sci Rep*. 2020;10(1):4637.

30. Harm W, Roider C, Jesacher A, Bernet S, Ritsch-Marte M. Lensless imaging through thin diffusive media. *Opt Express*. 2014;22(18):22146–22156.

31. Antipa N, Kuo G, Heckel R, Mildenhall B, Bostan E, Ng R, Waller L. Diffusercam: Lensless single-exposure 3d imaging. *Optica*. 2018;5(1):1–9.

32. Choi Y, Yoon C, Kim M, Yang TD, Fang-Yen C, Dasari RR, Lee KJ, Choi W. Scanner-free and wide-field endoscopic imaging by using a single multimode optical fiber. *Phys Rev Lett*. 2012;109(20):Article 203901.

33. Čižmár T, Dholakia K. Exploiting multimode waveguides for pure fibre-based imaging. *Nat Commun*. 2012;3:1027.

34. Di Leonardo R, Bianchi S. Hologram transmission through multi-mode optical fibers. *Opt Express*. 2011;19(1):247–254.

35. Papadopoulos IN, Farahi S, Moser C, Psaltis D. High-resolution, lensless endoscope based on digital scanning through a multimode optical fiber. *Biomed Opt Express*. 2013;4(2):260–270.

36. Sivankutty S, Andresen ER, Cossart R, Bouwmans G, Monneret S, Rigneault H. Ultra-thin rigid endoscope: Two-photon imaging through a graded-index multi-mode fiber. *Opt Express*. 2016;24(2):825–841.

37. Papadopoulos IN, Simandoux O, Farahi S, Huignard JP, Bossy E, Psaltis D, Moser C. Optical-resolution photoacoustic microscopy by use of a multimode fiber. *Appl Phys Lett*. 2013;102(21):Article 211106.

38. Mezil S, Caravaca-Aguirre AM, Zhang EZ, Moreau P, Wang I, Beard PC, Bossy E. Single-shot hybrid photoacoustic-fluorescent microendoscopy through a multimode fiber with wavefront shaping. *Biomed Opt Express*. 2020;11(10):5717–5727.

39. Bolshtyansky MA, Zel'dovich BY. Transmission of the image signal with the use of a multimode fiber. *Opt Commun*. 1996;123(4–6):629–636.

40. Mahalati RN, Gu RY, Kahn JM. Resolution limits for imaging through multi-mode fiber. *Opt Express*. 2013;21(2):1656–1668.

41. Valley GC, Sefler GA, Shaw TJ. Multimode waveguide speckle patterns for compressive sensing. *Opt Lett*. 2016;41(11):2529–2532.

42. Wang G, Mididoddi CK, Bai F, Gibson S, Su L, Liu J, Wang C. Ultrafast optical imaging using multimode fiber based compressed sensing and photonic time stretch. arXiv. 2018. https://arxiv.org/abs/1803.03061.

43. Amitonova LV, De Boer JF. Compressive imaging through a multimode fiber. *Opt Lett*. 2018;43(21):5427–5430.

44. Caravaca-Aguirre AM, Singh S, Labouesse S, Baratta MV, Piestun R, Bossy E. Hybrid photoacoustic-fluorescence microendoscopy through a multimode fiber using speckle illumination. *Apl Photonics*. 2019;4(9):Article 096103.

45. Guggenheim JA, Li J, Allen TJ, Colchester RJ, Noimark S, Ogunlade O, Parkin IP, Papakonstantinou I, Desjardins AE, Zhang EZ, et al. Ultrasensitive plano-concave optical microresonators for ultrasound sensing. *Nat Photonics*. 2017;11:714–719.

46. Simandoux O, Stasio N, Gateau J, Huignard J-P, Moser C, Psaltis D, Bossy E. Optical-resolution photoacoustic imaging

through thick tissue with a thin capillary as a dual optical-in acoustic-out waveguide. *Appl Phys Lett*. 2015;106(9):Article 094102.

47. Stasio N, Shibukawa A, Papadopoulos IN, Farahi S, Simandoux O, Huignard J-P, Bossy E, Moser C, Psaltis D. Towards new applications using capillary waveguides. *Biomed Opt Express*. 2015;6(12):4619–4631.

48. Fienup JR. Reconstruction of an object from the modulus of its fourier transform. *Opt Lett*. 1978;3(1):27–29.

49. Shnaiderman R, Wissmeyer G, Ülgen O, Mustafa Q, Chmyrov A, Ntziachristos V. A submicrometre silicon-on-insulator resonator for ultrasound detection. *Nature*. 2020;585:372–378.

50. Westerveld WJ, Mahmud-Ul-Hasan M, Shnaiderman R, Ntziachristos V, Rottenberg X, Severi S, Rochus V. Sensitive, small, broadband and scalable optomechanical ultrasound sensor in silicon photonics. *Nat Photonics*. 2021;15:341–345.